

MEASUREMENT OF THE INCLUSIVE JET AND DIJET CROSS SECTIONS
USING 2010 DATA FROM THE ATLAS DETECTOR AND CALIBRATION
STUDIES AND SIMULATION OF THE ATLAS FORWARD CALORIMETER

by

Peter Thompson

A thesis submitted in conformity with the requirements
for the degree of Doctor of Philosophy
Graduate Department of Physics
University of Toronto

Copyright © 2012 by Peter Thompson

Abstract

Measurement of the inclusive jet and dijet cross sections using 2010 data from the ATLAS detector and calibration studies and simulation of the ATLAS forward calorimeter

Peter Thompson

Doctor of Philosophy

Graduate Department of Physics

University of Toronto

2012

(At most 150 words for M.Sc. or 350 words for Ph.D.)

Contents

1	The LHC and the ATLAS Detector	1
1.1	The Large Hadron Collider	1
1.2	The ATLAS Detector	2
1.2.1	Coordinates	3
1.2.2	Inner Detector	4
1.2.3	Muon Spectrometer	7
1.2.4	Calorimetry	9
1.2.5	The ATLAS Calorimeters	14
1.2.6	Forward Calorimeters	20
1.2.7	Trigger and Data Acquisition	33
	Bibliography	42

List of Tables

1.1	Readout granularity for the EMEC [1]	19
1.2	Dimensions of the FCal modules.	24

List of Figures

1.1	Injection chain for protons and ions feeding the LHC.	2
1.2	Diagram of the ATLAS detector.	3
1.3	Diagram of the barrel section of the inner detector.	6
1.4	Diagram of the inner detector, showing the elements traversed by particles at pseudorapidity	
1.5	The different components of the Muon Spectrometer. The MDT and CSC components are us	
1.6	The calorimeters of the ATLAS detector.	15
1.7	Section of the electromagnetic barrel calorimeter, showing the accordion shape of the absorber	
1.8	Schematic view of the readout layer of an EM Barrel electrode, prior to folding. The piece on	
1.9	Schematic of a tile calorimeter module. Alternating layers of master plates and spacer plates	
1.10	photograph of an EMEC module, showing the accordion structure of the absorbers. The bou	
1.11	Electrode structure in the HEC. Electrodes are arranged to form an electrostatic transformer	
1.12	Cut-away view showing the FCal within its support tube[3]. The region inside the support tu	
1.13	Diagram showing the arrangement of electrodes and slugs in the hadronic modules [3].	23
1.14	Photo of an endplate of FCal1, taken during assembly, showing the interconnect board and th	
1.15	The FCal summing boards mounted on the rear of the HEC[3]	26
1.16	Diagram of the FCal readout chain for a single summed channel. Summed channels are comp	
1.17	Pulse shapes for each module. The dots indicate the times at which they are sampled and dig	
1.18	Calibration and ionisation pulse shapes for an EMB channel, after shaping. Prior to shaping,	
1.19	Distribution of charged particles produced in minimum bias events[5]. The plot shows data m	

Chapter 1

The LHC and the ATLAS Detector

1.1 The Large Hadron Collider

The Large Hadron Collider (LHC)[6] is a particle collider situated near Geneva, Switzerland. It is 27km in circumference and is located between 45m and 170m underground, crossing the Swiss-French border four times. It is designed to accelerate two beams of protons to energies of 7 TeV, and to collide these beams at four points along its circumference with instantaneous luminosities of up to $10^{34}\text{cm}^{-2}\text{s}^{-1}$. At present protons in the LHC are being accelerated to 4 TeV per beam, which is half of the design energy, while the instantaneous luminosity being achieved is currently around $\sim 8 \times 10^{33}\text{cm}^{-2}\text{s}^{-1}$. The LHC is also capable of accelerating heavy ions to high energy. The ALICE experiment is focused on analysing these heavy ion collisions, while both ATLAS and CMS also have heavy ion programs.

The injection chain for beam particles is shown in figure 1.1. Hydrogen gas is used as a source of protons. Gas molecules are ionised in a duoplasmatron[7], which emits protons at an energy of 90 keV. The protons are then accelerated to 750 KeV in a Radio Frequency Quadrupole (RFQ) before being accelerated to 50 MeV in a linear accelerator (LINAC2). A series of synchrotrons (the Proton Synchrotron Booster (PSB), Proton

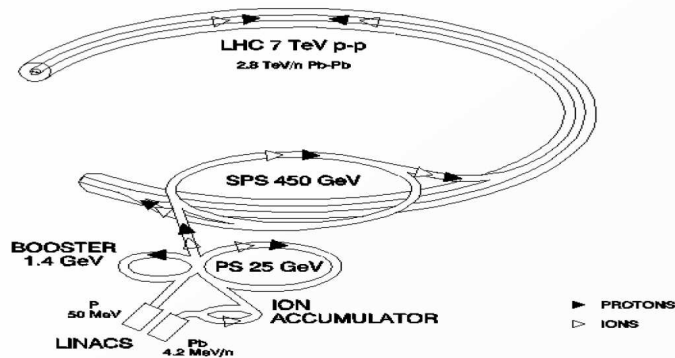


Figure 1.1: Injection chain for protons and ions feeding the LHC.

Synchrotron (PS), and Super Proton Synchrotron (SPS)) are then used to accelerate protons to energies of 1.4 GeV, 25 GeV and 450 GeV, respectively. After acceleration by the SPS, beams are injected into the LHC. The LHC beam is designed to hold up to 2808 bunches, each containing $\sim 10^{11}$ protons, which are separated in time by 25 ns. Superconducting Radio-Frequency (RF) cavities are then used to accelerate the protons to their final energy.

1.2 The ATLAS Detector

The ATLAS detector[1] (shown in figure 1.2) is a multi-purpose detector used to analyse collisions at the LHC. It is one of two multi-purpose detectors, the other being the Compact Muon Solenoid (CMS)[8]. It consists of sophisticated particle tracking systems, a system of calorimeters, and a Muon Spectrometer, each of which will be discussed below. The Inner Detector (ID) and Muon Spectrometer (MS) will be discussed only briefly, as they play little role in the analyses discussed in this thesis. This chapter will focus on the calorimeters of ATLAS, particularly the forward calorimeters.

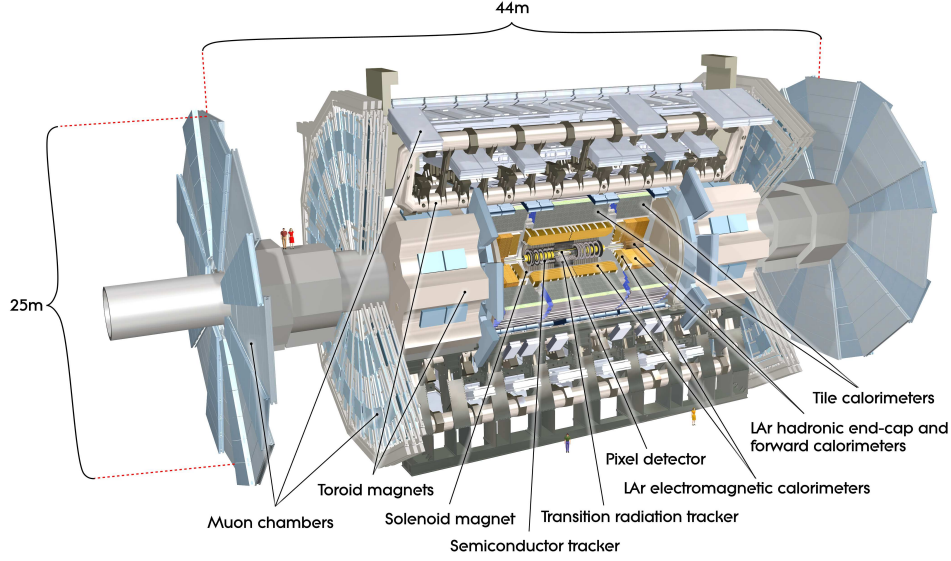


Figure 1.2: Diagram of the ATLAS detector.

1.2.1 Coordinates

ATLAS uses a right-handed Cartesian coordinate system. The nominal interaction point at the centre of ATLAS is defined to be the origin of this coordinate system, with the beams running along the z axis. The positive x axis points towards the centre of the LHC ring, while the positive y axis is perpendicular to the other two, and points upwards. Parts of the detector are labelled according to which side of the interaction point they are located on. The “A-side” refers to objects located at positive values of z , while objects located at negative z are said to be on the “C-side”. ATLAS is divided into a barrel and two end-cap sections. Each of these sections contains a cryostat, as (most of) the ATLAS calorimetry is based on liquid argon technology.

The polar angle θ defines the angle from the beam axis, while the azimuthal angle ϕ defines the angle around the beam axis. The direction $\theta = 0$ points along the positive z axis, while $\phi = 0$ corresponds to the positive x axis. The pseudorapidity, η , is defined

using the polar angle θ , such that

$$\eta = -\log \left(\tan \left(\frac{\theta}{2} \right) \right). \quad (1.1)$$

Pseudorapidity is an approximation to rapidity, y . The rapidity of an object with energy E is given by

$$y = \frac{1}{2} \log \left(\frac{E + p_z}{E - p_z} \right), \quad (1.2)$$

where p_z is the z component of the objects momentum. The rapidity may be used to define a boost along the z axis, such that in the boosted frame of reference the object's momentum will be perpendicular to the beam direction. In the limit where the mass of the object is negligible, pseudorapidity and rapidity are equivalent.

1.2.2 Inner Detector

The Inner Detector is used to reconstruct the trajectories (tracks) of charged particles produced during proton-proton collisions. It is comprised of three systems: the pixel detector, the SemiConductor Tracker (SCT), and the Transition Radiation Tracker (TRT). These three components are contained within a cylindrical region of length 3.5m and radius 1.15m centred on the **ATLAS** interaction point. The **ATLAS** solenoid is a superconducting magnet located just outside of the ID, and generates a 2T magnetic field oriented along the z axis in the region occupied by the ID. The applied field gives rise to curvature in the trajectories of charged particles, such that measurements of particle trajectories can be used to determine the transverse momentum (p_T) of those particles. The ID is also used for vertex reconstruction at **ATLAS**. The primary vertex is associated with the location of the hard inelastic collision, while other soft collisions may produce additional secondary vertices. The accuracy with which a given vertex position may be reconstructed is dependent on the number of tracks associated with the vertex and the p_T of those tracks. In cases where there are at least 70 tracks emerging from the primary

vertex and the quadratic sum of track p_T values exceeds 8 GeV, the primary vertex can be determined with an accuracy of $\sim 30 \mu\text{m}$ in the transverse plane and $\sim 50 \mu\text{m}$ in the longitudinal direction[9].

The inner detector consists of a barrel section (shown in figure 1.3) and two end-cap sections (figure 1.4).

The pixel detector uses sensors formed from $250\mu\text{m}$ thick wafers of silicon. The barrel section consists of three cylindrical layers, and three disc-like layers are used to form each end-cap. All together there are $\sim 8 \times 10^7$ pixel channels, providing a hit resolution of $10 \mu\text{m}$ in the $R - \phi$ plane and $115 \mu\text{m}$ in the z direction.

The SCT is located beyond the pixel detector, and consists of 4 cylindrical layers in the barrel section and 9 disc layers in each end-cap. Each SCT module has semiconducting microstrip sensors mounted on both sides. The sensors on either side are oriented at an angle of 40 mrad to each other. As a single microstrip sensor only provides a position measurement in one dimension, orienting two at a slight angle allows the position of the hit to be measured in two dimensions. This gives the SCT a resolution of $17 \mu\text{m}$ in the $R - \phi$ plane and $580 \mu\text{m}$ in z .

The TRT is the outermost section of the inner detector, and is formed from straw-shaped drift tubes. The barrel section contains $\sim 52,500$ tubes, while $\sim 123,000$ tubes are contained in each end-cap section. Straws are made from layers of polyimide, aluminium, polyurethane and graphite-polyimide. Each straw is 4mm in diameter, with a gold-plated tungsten wire (of diameter $31\mu\text{m}$) located in the centre of the tube that serves as an anode. The gas in the tubes is 70% Xe, 27% CO_2 and 3% O_2 . Charged particles entering the tube ionise the gas, with the resulting electrons drifting towards the anode in the centre. Measurement of the electron drift time allows the distance of the particle track from the wire to be determined with a resolution of $130\mu\text{m}$. The straw tubes are housed within a volume filled with CO_2 and a matrix of polypropylene fibres (in the barrel section) or foils (in the end-caps). Electrons moving between the CO_2 /polypropylene

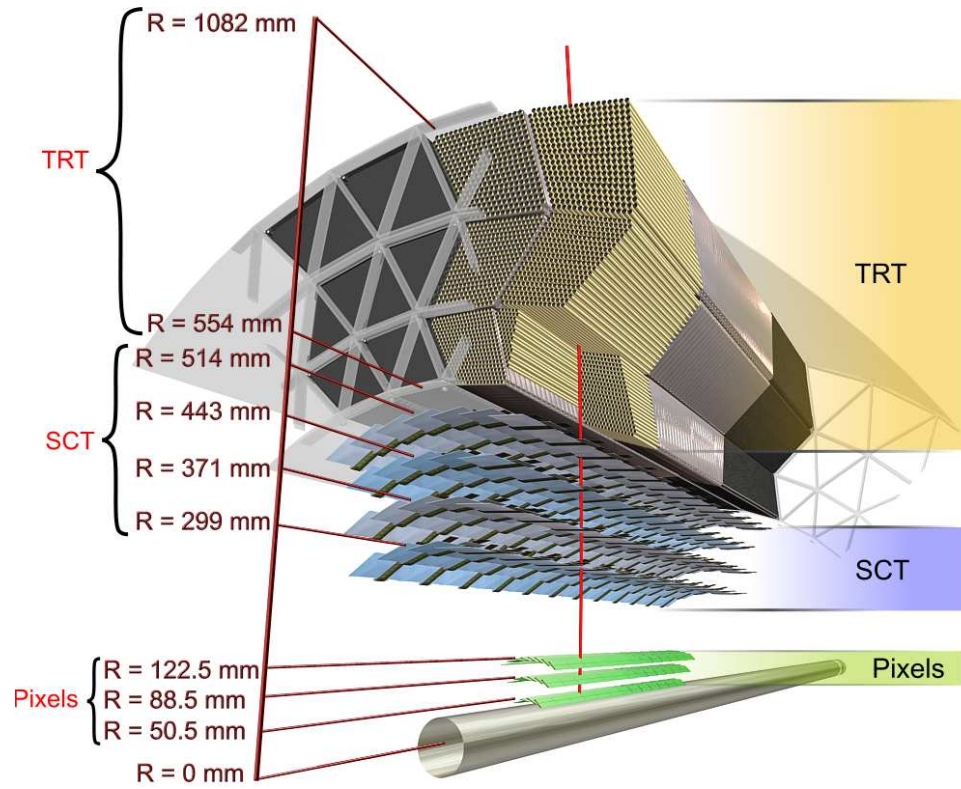


Figure 1.3: Diagram of the barrel section of the inner detector.

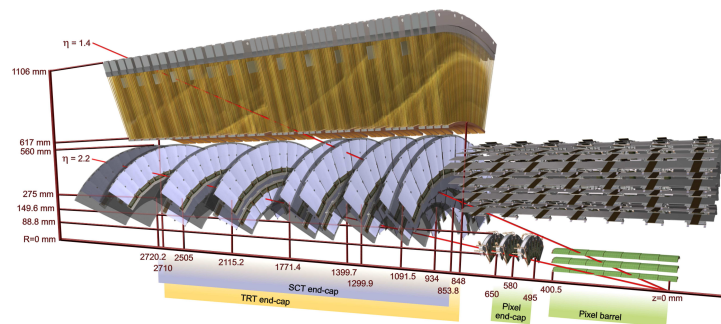


Figure 1.4: Diagram of the inner detector, showing the elements traversed by particles at pseudorapidities of 1.4 and 2.2.

interfaces emit transition radiation. This radiation (and the original electron) will then ionise the gas inside the tubes, inducing a signal on the tube anodes. Xenon is used because it efficiently absorbs the transition radiation photons, emitting photoelectrons in the process. Charged pions produce less transition radiation than electrons, and thus generate smaller signals. This difference in signal size allows the TRT to perform particle identification, discriminating electrons from charged pions.

1.2.3 Muon Spectrometer

The Muon Spectrometer is the outermost system of the ATLAS detector, and is illustrated in figure 1.5. It is designed to measure muons in the region $|\eta| < 2.7$ with a momentum resolution of $\sim 10\%$ at 1 TeV. although during 2010 running muons were measured with a resolution of $\sim 5\%$ at 100 GeV in the barrel region[10]. When the fit to this data is extrapolated, it corresponds to a resolution of $\sim 25\%$ at 1 TeV. The Muon Spectrometer is also capable of triggering on muons in the region $|\eta| < 2.4$. The Muon Spectrometer is comprised of four types of detectors: Monitored Drift Tubes (MDTs), Cathode Strip Chambers (CSCs), Resistive Plate Chambers (RPCs) and Thin Gap Chambers (TGCs). The MDTs and CSCs are referred to as “precision chambers” and are used to measure the kinematics of muons, while the TGCs and RPCs are used for triggering and measuring the ϕ coordinates of muon tracks.

Superconducting toroidal magnets (the barrel toroid and two end-cap toroids) are located beyond the calorimeters. These produce a toroidal field (i.e. one in which the field lines run in the azimuthal direction), which causes charged particles to bend in the $R - z$ plane. In order to measure track momenta with high resolution, the relative alignment of the MDT and CSC chambers must be well known. A high precision optical system is used to monitor the positions and mechanical deformations of the measurement chambers, which must be known to within $30 \mu\text{m}$ in order to achieve the desired momentum resolution.

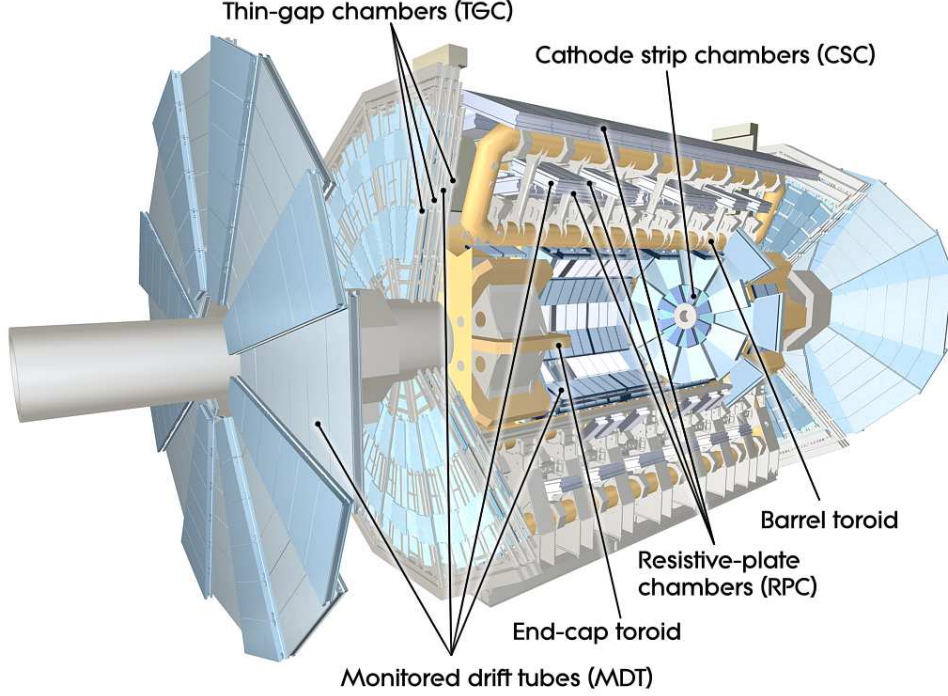


Figure 1.5: The different components of the Muon Spectrometer. The MDT and CSC components are used for measuring muon momenta, while the RPCs and TGCs are used primarily for triggering.

MDTs are comprised of cylindrical drift tubes of diameter 29.97mm, with a central anode wire of diameter $50\mu\text{m}$. A mixture of Argon (93%) and CO_2 (7%) is used to fill the tubes. Each drift tube is capable of measuring the distance of a muon track from the anode wire with a resolution of $80\mu\text{m}$. The tubes are grouped together to form chambers. There are three (roughly) cylindrical layers of chambers in the barrel (at radii of 5 m, 7.5 m and 10 m), and two layers in each end-cap.

In the end-cap sections, the innermost layer of precision measurement chambers is made up of CSCs, as the MDTs are unable to operate in the high levels of radiation present at these locations. The CSCs are multi-wire proportional chambers (MWPCs), filled with a mixture of Argon (80%) and CO_2 (20%), and are capable of measuring hit positions to within $60\mu\text{m}$ in the bending plane.

For triggering purposes, RPCs are used in the barrel region ($|\eta| < 1.05$) while TGCs

(which are a form of MWPC) are used in the end-cap region ($1.05 > |\eta| > 2.4$). The intrinsic response time of these detectors is on the order of a few nanoseconds, enabling them to reliably identify the bunch crossing in which any detected muons were produced.

1.2.4 Calorimetry

1.2.4.1 Sampling Calorimeters

All of the calorimeters used at ATLAS are sampling calorimeters, which consist of active regions and passive (absorbing) regions. The active layers are sensitive: energy deposited in these regions produces a signal which is then read out. The passive regions are made from a denser absorbing material, which is used to regulate the shower size. Sampling calorimeters are less expensive to produce than homogenous calorimeters, and tend to occupy less space: If a homogenous calorimeter can completely contain a shower in a given volume, then a sampling calorimeter made using the same active material will be able to contain the shower in a smaller volume.

Sampling calorimeters may be characterised by their sampling fraction, which is defined as the energy deposited in the active regions by a minimum ionising particle (MIP) divided by the total energy deposited in the active and passive regions by the mip [11].

Most of the ATLAS calorimeters are based on liquid argon (LAr) technology, i.e. LAr is used to form the active regions of the calorimeter. Charged particles passing through these active regions ionise the liquid argon. The liberated electrons then drift in an applied electric field, resulting in an induced current pulse. This current is then used as a signal.

The ATLAS Tile calorimeter uses tiles of scintillating polystyrene as the active material, which are positioned between layers of steel (the passive material). Charged particles passing through these tiles excite the scintillating material, which then produces photons. This scintillation light is then wavelength shifted in order to prevent it from being reab-

sorbed by the scintillating material, and then carried by optical fibres to photomultiplier tubes (PMTs), which absorb the light and produce an electrical signal.

1.2.4.2 Electromagnetic Shower Development

Photons and electrons interact with the calorimeter via electromagnetic (EM) processes. The dominant processes by which electrons (or positrons) lose energy while traversing the material of the calorimeter are ionisation and bremsstrahlung. At high energies bremsstrahlung dominates, while at lower energies ionisation is the dominant process. The critical energy, ϵ_c , is defined as the value of an electrons energy at which the rate of energy loss via ionisation is equal to the rate of energy loss from bremsstrahlung. This value is material dependent, but an approximation for solids and liquids is given by[11]

$$\epsilon_c = \frac{610\text{MeV}}{Z + 1.24} \quad (1.3)$$

where Z is the atomic number of the element being traversed.

The longitudinal extent of an EM shower may be expressed in terms of the radiation length, which is the distance over which an electron loses $\sim 63\%$ ($1 - e^{-1}$) of its energy via bremsstrahlung. The radiation length of a material may be approximated by[12]

$$X_0 = \frac{716.4 A}{Z(Z + 1) \log(287/\sqrt{Z})} \text{ gcm}^{-2}, \quad (1.4)$$

where Z is the atomic number of the element. Note that the expression has units of g cm^{-2} , and so should be divided by the density of the material in order to obtain a value with dimensions of length. In cases where the material is comprised of multiple elements, then the radiation length of the compound is given by

$$\frac{1}{X_0} = \sum_j \frac{w_j}{X_{0,j}}, \quad (1.5)$$

where the $X_{0,j}$ and w_j are, respectively, the radiation length and fraction (by mass) of the j -th element.

A similar quantity exists to describe the lateral extent of an EM shower. The Molière radius, ρ_M , is given by

$$\rho_M = X_0 \frac{21.2 \text{ MeV}}{\epsilon_c}. \quad (1.6)$$

Unlike the radiation length, the Molière radius doesn't have a strict physical meaning, although roughly 80 – 90% of an EM shower's energy is generally deposited within a cylinder of radius ρ_M [11].

The dominant processes for showering photons are pair production, Compton scattering and the photoelectric effect. At higher energies ($> \sim 10$ MeV) pair production is the most likely, though as the photon's energy decreases Compton scattering becomes more prevalent, while the photoelectric effect dominates at the lowest energies ($< \sim 1$ MeV). The average distance that a high energy photon travels before undergoing pair production is $9/7 X_0$.

Typically, EM showers consist of successive bremsstrahlung and pair production interactions. An initial electron will radiate, producing a photon. The photon will then undergo pair production, yielding an electron-positron pair in addition to the original electron. This process then repeats, with electrons and positrons radiating photons that then convert into additional electron-positron pairs. This continues until the electron/positron energies fall below the critical energy, at which point they are more likely to lose energy via ionisation than through further radiation. The energy of the initial electron is thus divided between all the electrons and photons produced during the shower, which then deposit their energy in the calorimeter via ionisation.

1.2.4.3 Hadronic Shower Development

While EM showers tend to be dominated by only a few processes, there are many more processes that may take place in a hadronic shower, making them more complex.

The longitudinal development of hadronic showers is characterised by the nuclear interaction length, λ_{int} , which describes the average distance that a hadron will travel in a material before interacting with a nucleus. In general, λ_{int} scales as $A^{1/3}$, where A is the mass number of the element being traversed.

Hadronic showers have an EM component and a non-EM component. Of the π mesons produced in hadronic interactions, roughly 1/3 are π^0 mesons. The decay $\pi^0 \rightarrow \gamma\gamma$ occurs very quickly (with a lifetime of $8.5 \times 10^{-17}\text{s}$), with a branching fraction of 99% [13]. Thus, almost all the π^0 's produced in hadronic showers go on to induce EM showers. At each interaction, some of the energy carried by the non-EM component is redirected into the EM component. As the energy of the initial hadron increases, the number of interactions (and thus the fraction of energy carried by the EM component) increases also. The energy carried by the EM component thus scales non-linearly with the energy of the initial hadron.

A feature of the non-EM component of hadronic showers is that not all of the energy of the incident hadron is visible to the calorimeter. For instance, when a showering hadron interacts with a nucleus and frees a number of nucleons, the binding energy required to release those nucleons is essentially lost: it is invisible to the calorimeter. Neutrons are produced in large quantities during nuclear interactions, and while these may undergo further nuclear interactions they will not ionise the active region of the calorimeter, and so in that sense are invisible. Furthermore, nuclear reactions may produce particles that decay to muons and/or neutrinos. Muons (unlike electrons) deposit a minimal amount of energy via ionisation before leaving the calorimeter, while neutrinos leave the calorimeter without interacting at all (usually).

A calorimeter will have a lower response to a hadronic shower than it would to an EM shower of the same initial energy, unless it somehow corrects for this invisible energy. This correction is referred to as compensation. The most effective way to achieve compensation is by increasing the calorimeter's response to the non-EM shower component. This

response may be boosted if the active material contains hydrogen (as is the case with scintillating materials). In this case, the neutrons produced in nuclear interactions can scatter off hydrogen nuclei. The active material is then sensitive to the recoiling proton [14]. Alternatively, using fissile material as an absorbing material can boost the non-EM response. Energy released in fission reactions can compensate for invisible energy losses. The ZEUS[15] calorimeter is based on uranium/scintillator technology, and is an example of a compensating calorimeter.

The ATLAS calorimeters are all non-compensating, and thus the response of the calorimeters to hadrons is lower than for electrons of the same energy. Software-based methods are used during offline reconstruction to correct for this effect, as described in sections ?? and ??

1.2.4.4 Energy Resolution

The performance of a sampling calorimeter may be characterised in terms of its resolution, σ/\bar{E} , where \bar{E} is the mean reconstructed energy and σ is the RMS of the calorimeter response. The resolution is typically parameterised by a function of the form

$$\frac{\sigma}{\bar{E}} = \frac{A}{\sqrt{\bar{E}}} \oplus B \oplus \frac{C}{\bar{E}}, \quad (1.7)$$

where A , B , and C are called the stochastic, constant, and noise terms, respectively, and \oplus denotes that the term should be added in quadrature.

The stochastic term arises from variations in the sampled energy, for example, an incident particle may shower in a way that deposits a large amount of energy in the active regions of the calorimeter, or in a way that deposits less energy in these regions. These sampling fluctuations are governed by Poissonian statistics, and thus give rise to a term proportional to $\bar{E}^{-1/2}$ in the resolution[16].

The noise term is associated with electronic noise in the readout chain. For the liquid

argon calorimeters used at ATLAS, the majority of this noise is introduced in the preamplifiers which are located on the front end boards. The noise contribution is independent of the signal being read out of the channel, and so the noise term in the resolution scales as \overline{E}^{-1} .

The constant term arises from effects that are independent of energy deposited in the detector, such as nonuniformities in the calorimeter response. These nonuniformities may be caused by uninstrumented material in front of the calorimeter, irregularities in the calorimeter structure, or damage caused by radiation or aging, or a calorimeter design in which the response is dependent on the impact point of the incident particle. This impact point dependence forms the dominant contribution to the constant term for the forward calorimeters of ATLAS, which is discussed further in section ??.

1.2.5 The ATLAS Calorimeters

ATLAS contains five distinct calorimeters, shown in figure 1.6. The Electromagnetic Barrel (EMB) Calorimeter is located in the central “barrel” section of ATLAS, while the Electromagnetic End-cap Calorimeter (EMEC), Hadronic End-cap Calorimeter (HEC) and Forward Calorimeters (FCal) are located within the end-caps at either end. The Tile calorimeter consists of barrel section, and two extended barrel sections that surround the end-cap cryostats.

1.2.5.1 Barrel Calorimeters

The EM Barrel (EMB) calorimeter is a lead/liquid argon sampling calorimeter covering the pseudorapidity range $0 < |\eta| < 1.475$. Liquid argon was chosen for the active medium because it can be used to obtain a fast, linear response while also being resistant to radiation [1]. The absorber plates are folded into a distinctive accordion shape, as shown in figure 1.7. The shape of the absorber plates gives the EMB calorimeter a structure that is completely symmetric in the azimuthal direction, with no gaps in detector coverage.

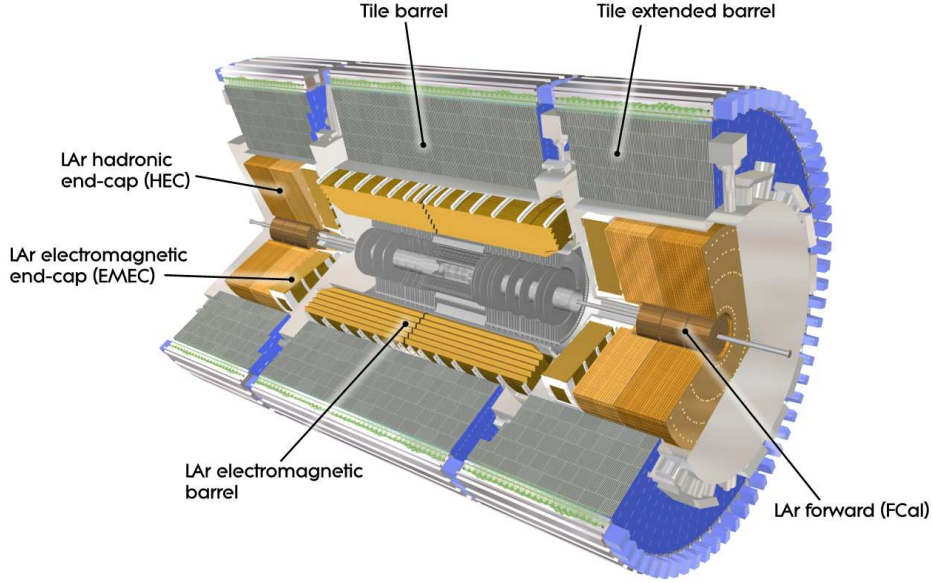


Figure 1.6: The calorimeters of the ATLAS detector.

The linearity and resolution of the response are thus uniform in ϕ .

The absorber plates are made of lead, with stainless steel sheets glued on each side in order to increase their mechanical strength. The plates are then folded into the accordion shape, with the folding angle increasing with depth (radius) in order to maintain the size of the LAr gap (and hence the sampling fraction) throughout the calorimeter. The lead plates are 1.5mm thick for $|\eta| < 0.8$ and 1.1 mm thick for $|\eta| > 0.8$. Thinner sheets are used at higher $|\eta|$ in order to control the depth of the calorimeter[17], which varies from 22 - 30 X_0 in the region $0 < |\eta| < 0.8$, and from 24 to 33 X_0 in the region $0.8 < |\eta| < 1.3$.

Flexible Printed Circuit Boards (PCBs) are used to form the electrodes, which consist of three layers of copper separated by polyimide. The electrodes are positioned in between layers of the absorber, with honeycomb spacers being used to keep the electrodes in the centre of these gaps. The absorber layers are grounded, while the two outer layers of copper on each electrode are connected to an HV supply at +2kV [1]. This creates two active liquid argon gaps of thickness 2.1 mm on either side of the electrode. The inner layer of copper on each electrode is used to read out the signal, as it is capacitively

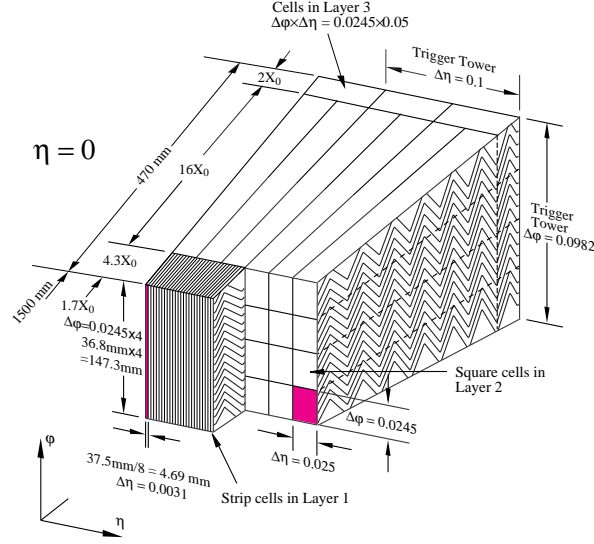


Figure 1.7: Section of the electromagnetic barrel calorimeter, showing the accordion shape of the absorber plates.

coupled to both the outer layers.

The readout of the EM Barrel calorimeter [2] is divided longitudinally (i.e. in depth) into three layers. The first and third layers are each a few X_0 in depth and only contain the beginning and end of the shower, while most of the energy is deposited in the second layer which has a depth of $\sim 17-20 X_0$. The readout granularity in $\Delta\eta \times \Delta\phi$ is 0.003×0.1 , 0.025×0.0245 , and 0.05×0.0245 in layers 1, 2 and 3, respectively. A diagram of the readout layer of the electrode is shown in figure 1.8, in which the different readout granularities are visible. The first layer has a very fine segmentation in η , which allows decaying π^0 particles to be distinguished from individual photons.

A steel/scintillator “Tile” calorimeter [18] is used to measure the energy of hadronic particles in the barrel region. It consists of a central barrel section covering the pseudo-rapidity range $|\eta| < 0.8$, and two extended barrel sections that enclose the LAr end-caps. The Tile calorimeter receives less radiation than the EM Barrel, and so alternatives to liquid argon based calorimetry are viable in this region. A steel/scintillator calorimeter was chosen as it was the most cost effective way of building a hadronic calorimeter with a large depth[1]. The total depth of the Tile calorimeter is 7.4 interaction lengths.

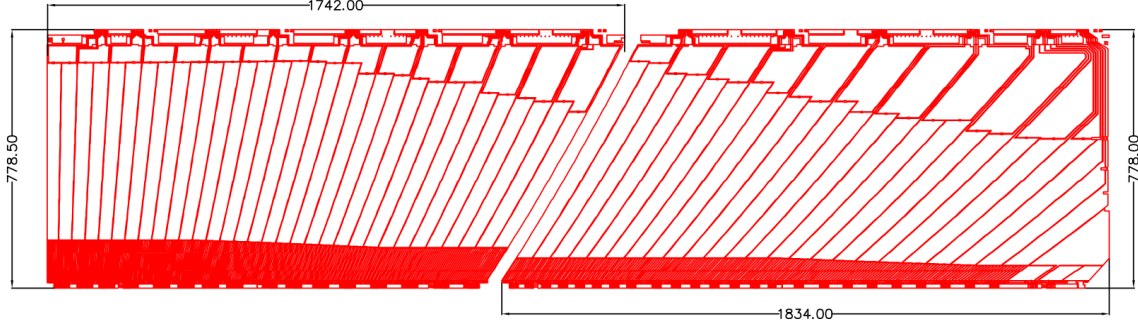


Figure 1.8: Schematic view of the readout layer of an EM Barrel electrode, prior to folding. The piece on the left is used to read out signals from $0 < \eta < 0.8$, while the piece on the right covers the region $0.8 < \eta < 1.475$ [2].

Each section of the Tile calorimeter is divided into 64 modules, each of which covers an azimuthal angle of 5.625° . The absorbing material of the calorimeter is formed from a series of steel “master” plates, which are 5mm thick and run the full radial depth of the tile calorimeter (2.0m). A series of smaller, 4mm thick spacer plates are positioned in between layers of master plates. The spacer plates are used to create gaps between adjacent master plates, and it is within these gaps that the scintillating tiles are located, as shown in figure 1.9. The scintillating tiles are made of polystyrene, which produces scintillation light in the ultra-violet range when excited by the passage of showering particles. The polystyrene is doped with fluors that shift the wavelength of this light into the visible spectrum. Optical fibres are coupled to two sides of each scintillator tile, and are used to carry light from the tiles to the Photomultiplier tubes (PMTs), which are housed within the mechanical support structure of the calorimeter. The PMTs then convert the scintillation light to an electronic signal.

1.2.5.2 End-Cap Calorimeters

The Electromagnetic End-Cap (EMEC) and Hadronic End-Cap (HEC) Calorimeters are liquid argon calorimeters housed within the end-cap cryostats at either end of the detector.

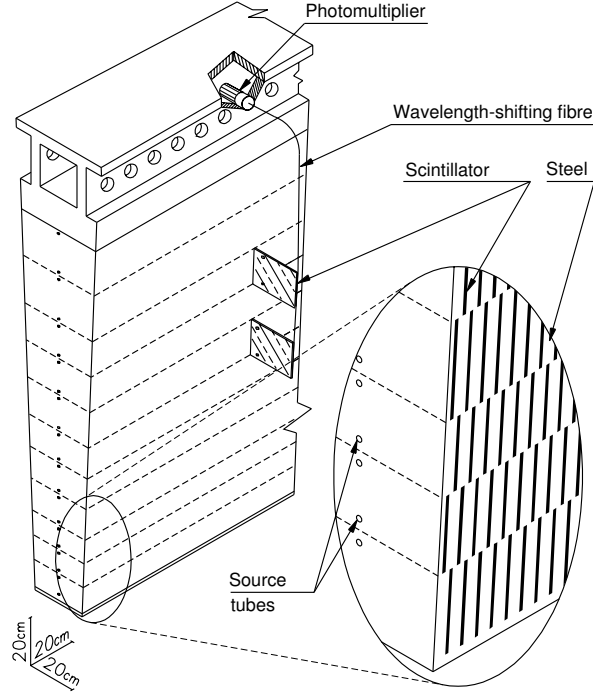


Figure 1.9: Schematic of a tile calorimeter module. Alternating layers of master plates and spacer plates are glued together, with scintillating tiles positioned in the gaps in this structure.

The EMEC covers the pseudorapidity range $1.375 < |\eta| < 3.2$, and has a similar design to the EM Barrel calorimeter. As with the barrel, the absorber is formed from accordion shaped layers of lead sheets, while the active regions consist of the liquid argon gaps between these layers. Honeycomb spacers are used to keep the electrodes positioned in the centres of these gaps. A module of the EMEC is shown in figure 1.10.

The EMEC consists of two coaxial wheels, with the boundary between wheels located at $|\eta| = 2.5$, matching the acceptance of the ID. The inner wheel uses absorber sheets of thickness 2.2mm, giving the calorimeter a depth of $26 - 36X_0$ in the region $2.5 < |\eta| < 3.2$, while the absorber plates in the outer wheel are thinner (1.7mm) giving the calorimeter a depth of $24 - 34X_0$ in this region. Each wheel is subdivided into eight wedge-shaped modules. Due to the accordion shape of the absorber layers, there are no discontinuities in the calorimeter between adjacent modules. As with the EM barrel, the structure of



Figure 1.10: photograph of an EMEC module, showing the accordion structure of the absorbers. The boundary between the inner wheel and the outer wheel can be seen towards the left, where the shape of the absorber plate changes.

the EMEC is completely symmetric with respect to azimuthal angle. The number of readout layers and their granularities are dependant on pseudorapidity; this information is summarised in table 1.1.

pseudorapidity	layer 1	layer 2	layer 3
$1.375 < \eta < 1.425$	0.050×0.1	0.050×0.025	-
$1.425 < \eta < 1.5$	0.025×0.1	0.025×0.025	
$1.5 < \eta < 1.8$	0.0031×0.1		
$1.8 < \eta < 2.0$	0.0042×0.1		
$2.0 < \eta < 2.4$	0.0063×0.1		
$2.4 < \eta < 2.5$	0.025×0.1		
$2.5 < \eta < 3.2$	0.1×0.1	0.1×0.1	-

Table 1.1: Readout granularity for the EMEC [1]

The HEC calorimeters [19] utilise a parallel plate geometry, which consists of alternating layers of copper and liquid argon oriented at right angles to the beam. Each side of the HEC consists of front wheel and a rear wheel, each of which is divided azimuthally into 32 wedge-shaped modules. The front wheel is comprised of a front plate which is

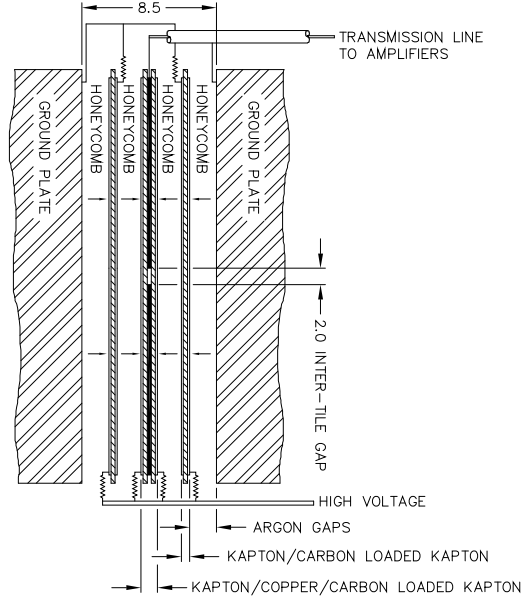


Figure 1.11: Electrode structure in the HEC. Electrodes are arranged to form an electrostatic transformer

12.5 mm thick, as well as 24 copper plates, each of which is 25mm thick. The rear wheel contains a front plate that is 25mm thick, and is followed by 16 plates of thickness 50mm.

In both wheels, the liquid argon gaps formed between the absorber plates have a depth of 8.5mm. These gaps are divided into four sub-gaps of depth ~ 2 mm by a set of three parallel electrodes, forming an electrostatic transformer [20]. The signal is read off a central pad in the middle electrode, with shapes etched into this pad determining the read-out structure. Cells in the HEC have a granularity of 0.1×0.1 in $\Delta\eta \times \Delta\phi$ for $|\eta| < 2.5$, and 0.2×0.2 at higher $|\eta|$.

1.2.6 Forward Calorimeters

The ATLAS Forward Calorimeters (FCal) are located just outside the beampipe, with their front faces situated 4.7 m from the ATLAS interaction point on either side. These

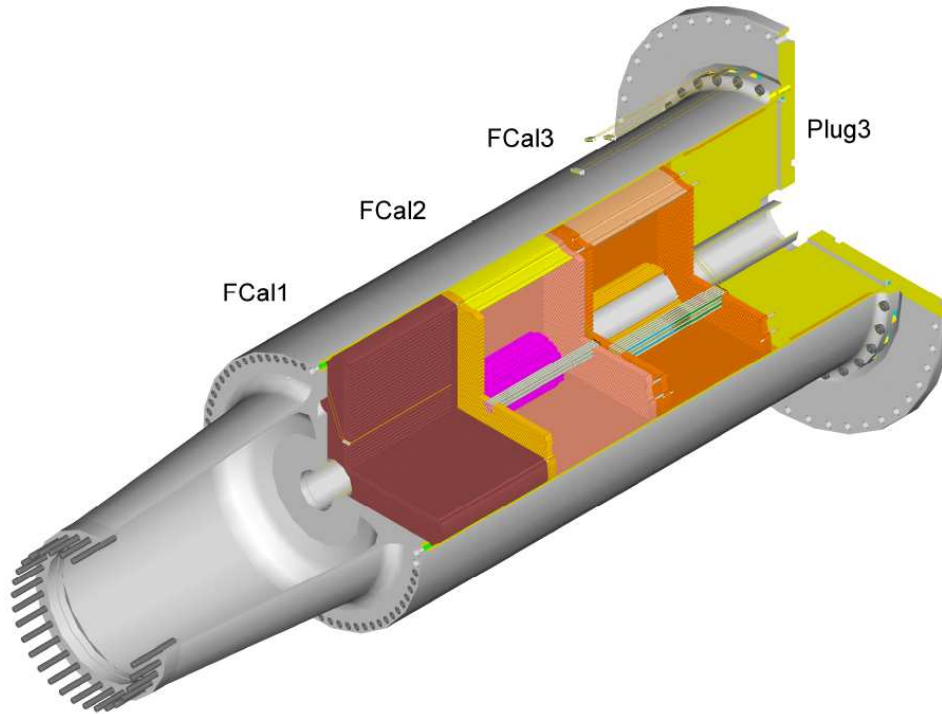


Figure 1.12: Cut-away view showing the FCal within its support tube[3]. The region inside the support tube and just upstream of the calorimeter is evacuated in ATLAS.

are liquid argon based calorimeters, and are located within a support tube inside the end-cap cryostat (figure 1.12).

Each FCal consists of three modules, one electromagnetic module (FCal1) and two hadronic modules (FCal2 and FCal3). Each module has a cylindrical shape, with an outer radius of 449 mm and a depth of 444 mm. A plug made of a brass alloy has a similar shape and is located behind the hadronic modules in order to provide additional shielding for the muon chambers behind it. As the FCal operates at a temperature just below 90K in ATLAS, “cold” values will be used in the following when quoting dimensions, densities, or other temperature-dependent quantities.

The electromagnetic modules of the FCal were produced by the university of Arizona. Each module consists of a stack of circular copper plates with an inner radius of 72 mm and an outer radius of 449 mm. Each plate is drilled with a hexagonal array of holes

into which the electrodes were inserted. This was done in a way that established a good electrical connection between the outside of the electrode and one of the copper end-plates. Each electrode consists of a copper tube (the cathode) containing a copper rod (anode) around which a radiation-hard PEEK fibre is wrapped. The inner radius of the copper tubes is 2.62 mm while the radius of the copper rods is 2.35mm, thus leaving a gap of $267\text{ }\mu\text{m}$ which is filled with liquid argon. The PEEK fibre has a diameter of $250\text{ }\mu\text{m}$, and is present to keep the rod positioned in the centre of the tube, thus maintaining the uniformity of the LAr gap throughout the electrode and keeping the rod electrically isolated from the tube. Typical gap sizes used in traditional LAr calorimeters are on the order of a few millimetres, as is the case for the EM Barrel, EMEC and HEC calorimeters. However, as the FCal is located at high pseudorapidity, minimum bias events will deposit energy in it at a very high rate. The smaller gap size is required in order to reduce the drift time across the gap, and thus preventing the high rate of ionisation from causing a build-up of positive ions in the liquid argon. Positive ion buildup can distort the electric field in the LAr gap, thus distorting the signal from the electrode. The distance between electrodes in FCal1 is similar to the Molière radius for copper. EM showers in the FCal should thus spread across several electrodes, allowing the calorimeter to sample the shower effectively. Copper also allows the FCal1 module to conduct heat efficiently. The cryostat temperature is kept at 88.5K, while the boiling point for liquid argon within the cryostat is 92.7K. With the LHC running at design luminosity, minimum bias events are expected to heat the FCal at a rate of about 45W, with about half of that power going into FCal1. A finite element analysis estimated that this heating would cause a temperature increase within the FCal of no more than 1.5K, which is not enough to cause the liquid argon to boil[3].

The hadronic modules of the FCal were produced at the University of Toronto (FCal2) and at Carleton University in Ottawa (FCal3). They have a similar design to the electromagnetic module, however tungsten is used as the absorber material instead of copper.

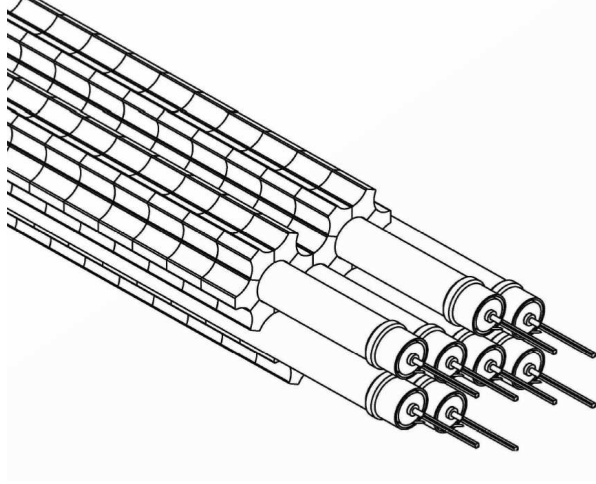


Figure 1.13: Diagram showing the arrangement of electrodes and slugs in the hadronic modules [3].

Each of the hadronic modules uses two copper end plates drilled with a hexagonal array of holes, each of which holds an electrode. The electrodes use copper tubes for their cathodes and rods made of pure tungsten (with density 19.2 g/cm^3) for the anodes. The absorber matrix is formed from small slugs of tungsten alloy (“WFeNi” - 97% tungsten/2% Iron/1% Nickel) positioned in the gaps between the electrode tubes, as shown in figure 1.13. The material composition and density of the calorimeter components are important factors when establishing a description of the calorimeter to be used by simulations. By themselves, the WFeNi slugs have a measured mean density of 18.3 g/cm^3 . When considering the WFeNi slugs, the copper electrode tubes, and any spaces in the absorber matrix that are filled with liquid argon, the average density of absorbing material in the hadronic modules is estimated to be 14.33 g/cm^3 for FCal2 and 14.45 g/cm^3 for FCal3 [21].

1.2.6.1 FCal Electronics

An electric field of $\sim 1 \text{ KV/mm}$ is conventional for liquid argon calorimeters. In order to provide this the rods of each electrode are supplied with high voltage while the tubes are grounded. Showering particles ionise the liquid argon, leaving free electrons and Ar^+

quantity	FCal1	FCal2	FCal3
Absorber material	Copper	Tungsten	Tungsten
Module inner diameter	72 mm	79 mm	86 mm
Electrode Separation	7.5mm	8.62 mm	9.0mm
Rod Diameter	2.35 mm	2.47 mm	2.75 mm
Tube inner diameter	2.62 mm	2.84 mm	3.25 mm
LAr Gap	267 μm	375 μm	500 μm
Distance from IP to front face	4668.5mm	5128.3 mm	5602.8
Number of electrodes	$\sim 12,000$	$\sim 10,000$	~ 8000

Table 1.2: Dimensions of the FCal modules.

ions in the gap. The electric field in the gap then causes this charge to drift resulting in a current pulse. This pulse is triangular in shape, having a fast rise time (~ 1 ns) and taking ~ 61 ns (in FCal1) to return to zero [3]. The height of the pulse peak depends on the amount of charge deposited in the liquid argon, and is thus proportional to the amount of energy deposited in the liquid argon ¹.

The signal is read out via a coaxial cable that also supplies the electrodes with high voltage. Electrodes in the FCal are ganged together on interconnect boards to form “tube groups”. Tube groups are formed from four electrodes in FCal1, six electrodes in FCal2, and nine electrodes in FCal3. Gold-plated signal pins connect the rods from these electrodes to the interconnect board, which is supplied with HV via a coaxial cable as shown in figure 1.14. The tubes are also grounded through this coax: each interconnect board is connected (via grounding pins) to the FCal end plate. As the interconnect board connects electrodes in parallel, the signal carried off the interconnect board is the sum of the current pulses in each electrode of that tube group.

The readout lines are then fed out to summing boards, which are located on the rear of the HEC (i.e. inside the end-cap cryostats) as shown in figure 1.15. On each summing board, signals from four interconnect boards are further combined to form a single readout channel. A typical FCal channel thus corresponds to four tube groups, which is equivalent

¹The energy required to ionise an atom of argon is 15.8 eV.

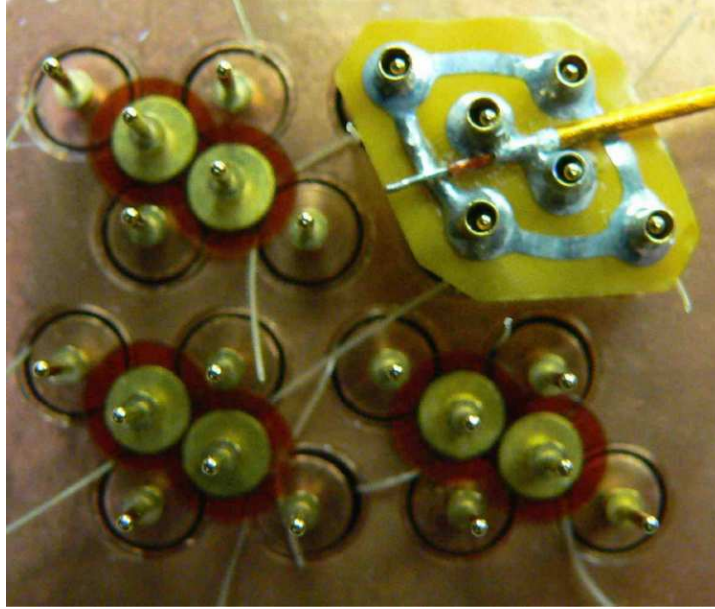


Figure 1.14: Photo of an endplate of FCal1, taken during assembly, showing the interconnect board and the coaxial cable used for HV delivery and readout [3]. Also visible are the PEEK fibres used to keep the rods centred within the tubes. The two central pins in each group are used to ground the end plate, and thus the tubes, while the four exterior pins provide HV to the rods and carry the signal off the electrode.

to 16/24/36 electrodes in FCal1/FCal2/FCal3. The summing is carried out through a transmission line transformer, which serves to match the impedance of the readout coax to that of the “pigtail” cable used to carry the signal away from the summing board (figure 1.16). A different HV source is used to supply each tube group in a given channel, so that if one source fails then the other three tube groups in the channel should still be powered. This has occurred in *ATLAS*: one of the lines supplying HV to the A side of the FCal was severed during installation. This line supplies HV to one quadrant of FCal3, leaving one quarter of the tube groups in the affected area without HV. The remaining tube groups still contribute signal to the channels in this area, and so the effect of the severed HV line is corrected for during reconstruction.

Near the inner and outer edges of the FCal the tube groups are irregularly shaped. It is not feasible to sum these channels in a coherent manner, and these “unsummed”



Figure 1.15: The FCal summing boards mounted on the rear of the HEC[3]

channels also provide better readout granularity at high $|\eta|$.

“Pigtail” cables are used to carry the signal from the summing boards to the cryostat feedthrough. Outside the cryostat, a stripline cable is used to carry the signal from the feedthrough to the Front End Boards.

1.2.6.2 Front End Boards

Front End Boards (FEBs)[22] are used in the electronics chains of all liquid argon calorimeters. Much of the following discussion applies to the electronics associated with all of these calorimeters, however some of the details mentioned here are specific to the electronics chain of the FCal.

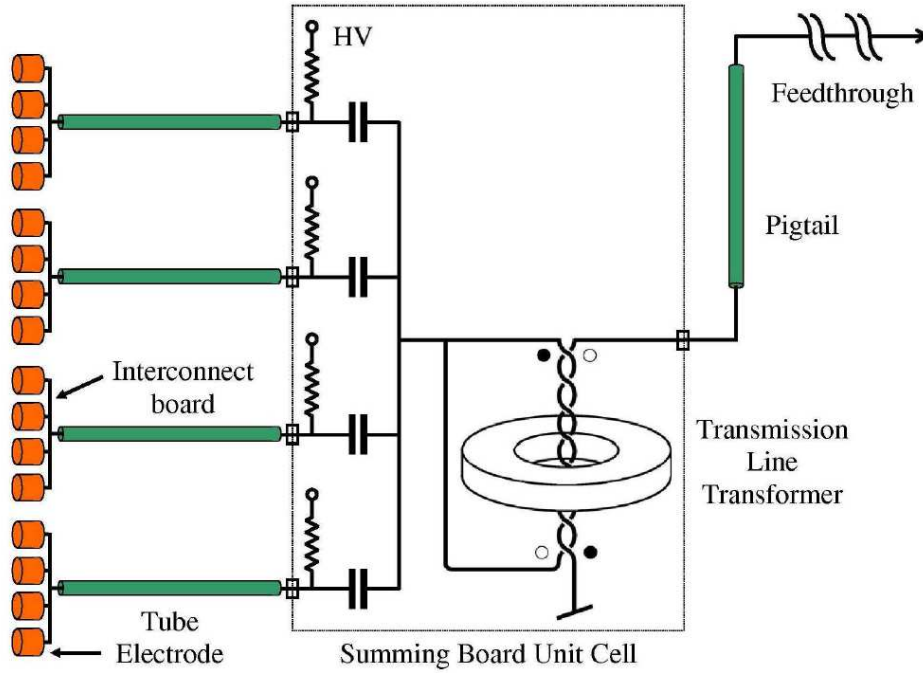


Figure 1.16: Diagram of the FCal readout chain for a single summed channel. Summed channels are composed of four tube groups, which each consist of 4/6/9 electrodes in FCal1/FCal2/FCal3.

On the FEB, the signal is amplified and then shaped. The shaping consists of one differentiation and two integration steps ($CR\text{-}RC^2$) resulting in a bipolar pulse shape. This is done in order to optimise the signal with respect to pileup and electronics noise[17, 22]. In the other LAr calorimeters it takes much longer for the triangular current pulse to drop from its peak value back to zero due to the larger gap size: this time is ~ 400 ns in the EM barrel but only ~ 60 ns in the FCal1 [3]. In these cases the shaping also allows the signal to be read out much faster, as the relevant information can be obtained from the first ~ 125 ns of the shaped pulse. Three different gains (low, medium, and high) are used when amplifying the signal. The amplification used for high gain is about 10 times as much as that used for medium gain, which in turn is about 10 times higher than that used for low gain. Each shaping chip processes the signals from four channels. An additional output on this chip sums the four inputs and then shapes the result. This

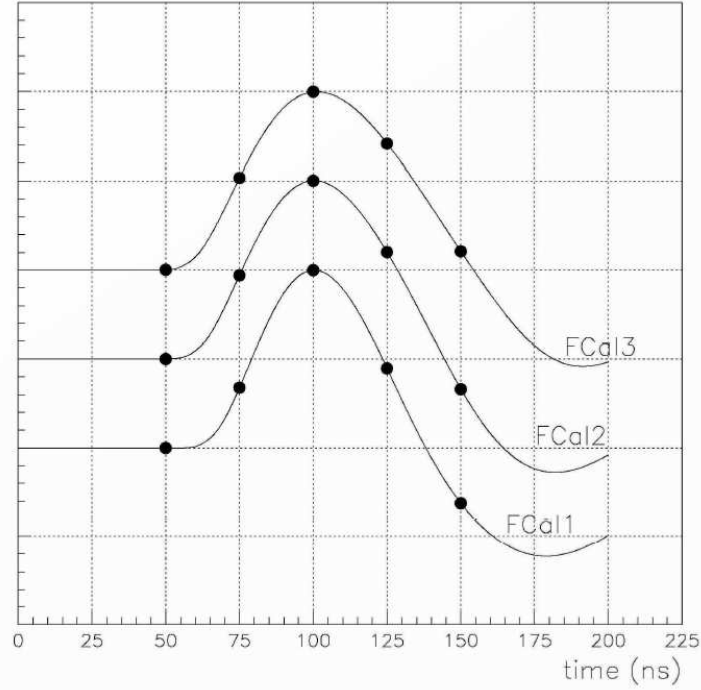


Figure 1.17: Pulse shapes for each module. The dots indicate the times at which they are sampled and digitised.

output is used in the formation of trigger towers, which are discussed in section 1.2.7.

Timing on the FEB is managed by a Trigger Timing Control (TTC) chip, which distributes clock pulses every 25ns. The signal (at each gain) is sampled at every 25ns, and stored (as an analog voltage) on a Switched Capacitor Array (SCA) circuit. The pulse shapes for the three FCal modules are illustrated in figure 1.17, showing the times at which the signals are sampled. Each pulse consists of an initial positive lobe followed by a longer negative lobe, the start of which can be seen in the figure.

When a trigger signal indicates that an event should be read out, the pulse samples are read off the SCA and fed to an ADC (Analog to Digital Converter). For each sample the ADC then outputs a 12-bit signal, which is a discretised voltage capable of taking one of 4,096 distinct levels. Under normal operation only a single gain is read out of the SCA and digitised, and so a gain selector chip is used to determine which gain will yield the largest pulse height without saturating the ADC output. In order to represent

a negative value, such as samples taken on the negative lobe of the pulse, a “pedestal” value is subtracted from the digitised output. To balance this, an offset is added to the samples read from the SCA just prior to them being digitised[22]. The offset voltage is chosen such that the pedestal value is around 1,000 ADC counts, leaving around 3,000 ADC counts to represent the positive lobe of the pulse. In *ATLAS*, the pedestal values for each channel are obtained from electronic calibration runs. For the testbeam studies discussed in chapter ?? the pedestal values were obtained from physics data on a run by run basis. For each channel, the first sample of each pulse was averaged over the entire run, and this value was used as the pedestal during reconstruction.

1.2.6.3 Signal Reconstruction/Optimal Filtering Method

Offline reconstruction of the energy deposited in the calorimeter is done through the use of optimal filtering coefficients (OFCs) [23]. These coefficients are used to reconstruct the amplitude of the signal pulse and its timing in such a way that the effect of the noise on the reconstruction is minimised.

The OFC method produces two sets of coefficients, a_i and b_i , which on average correctly produce the pulse amplitude A and time shift τ :

$$A = \left\langle \sum_i a_i S_i \right\rangle \quad (1.8)$$

$$A\tau = \left\langle \sum_i b_i S_i \right\rangle, \quad (1.9)$$

where S_i is the value of the i -th signal sample, after pedestal subtraction. Given that the pulse shape, $g(t)$ is known, these samples may be expressed as

$$S_i = Ag(t_i - \tau) + n_i = Ag(t_i) - A\tau g'(t_i) + n_i, \quad (1.10)$$

where g' is the derivative of the pulse shape and n_i is the noise present in the i -th sample.

Equations 1.8 and 1.9 may then be rewritten as

$$A = \sum_i a_i A g(t_i) - a_i A \tau g'(t_i) + a_i \langle n_i \rangle \quad (1.11)$$

$$A \tau = \sum_i b_i A g(t_i) - b_i A \tau g'(t_i) + b_i \langle n_i \rangle \quad (1.12)$$

The coefficients should be chosen in such a way that the variances of A and $A \tau$ are minimised. As the mean value of the noise is zero, these variances may be written as

$$\text{Var}(A) = \sum_{i,j} a_i a_j \langle n_i n_j \rangle \quad (1.13)$$

$$\text{Var}(A \tau) = \sum_{i,j} b_i b_j \langle n_i n_j \rangle, \quad (1.14)$$

where $\langle n_i n_j \rangle$ is simply the autocorrelation matrix of the noise between samples. This minimisation may be carried out using the method of Lagrange multipliers, with constraints

$$\begin{aligned} \sum_i a_i g_i &= 1, & \sum_i a_i g'_i &= 0 \\ \sum_i b_i g_i &= 0, & \sum_i b_i g'_i &= -1 \end{aligned}$$

obtained from equations 1.11 and 1.12.

For the testbeam studies discussed in chapter ??, a SPICE [24] simulation of the FCal electronics chain is used to obtain an initial estimate of the pulse shape used in the OFC calculation. This estimate was then improved using an iterative procedure that incorporated data taken from testbeam runs. The data used in this procedure are taken from events in which have a large pulse amplitude, in order to ensure that the signal is coming from a physical energy deposit.

1.2.6.4 Electronic Calibration

After reconstructing the pulse amplitude, an “ADC2MeV” factor is applied in order to convert the pulse amplitude (in ADC counts) to the energy deposited in the calorimeter

cell. For the FCal, the ADC2MeV value used during reconstruction is obtained from test-beam measurements (see section ??), while for the other LAr calorimeters an electronic calibration procedure is used to obtain the ADC2MeV factor.

The ADC2MeV factor may be written as the following product:

$$F_{\text{ADC} \rightarrow \text{MeV}} = F_{\mu\text{A} \rightarrow \text{MeV}} F_{\text{DAC} \rightarrow \mu\text{A}} \frac{1}{M_{\text{phys}}/M_{\text{calib}}} R. \quad (1.15)$$

The factors $F_{\text{DAC} \rightarrow \mu\text{A}}$, R , and $\frac{1}{M_{\text{phys}}/M_{\text{calib}}}$ are derived from electronic calibration studies of the calorimeter, and will be discussed below. The factor $F_{\mu\text{A} \rightarrow \text{MeV}}$ describes the amount of energy that must be deposited in the calorimeter cell in order for the signal current in the calorimeter electrodes to have a peak value of 1 μA . Note that $F_{\mu\text{A} \rightarrow \text{MeV}}$ is related to the sampling fraction, f_{samp} , of the calorimeter, such that

$$\frac{1}{F_{\mu\text{A} \rightarrow \text{MeV}}} = \frac{f_{\text{samp}}}{\tau_{\text{drift}} E_{\text{ion}}}, \quad (1.16)$$

where E_{ion} is the ionisation energy of argon (15.8 eV) and τ_{drift} is the electron drift time in the calorimeter cell.

All of the liquid argon calorimeters in ATLAS make use of a calibration board, which injects a calibration pulse into the readout chain. In the FCal, this pulse is injected at the input to the FEB, whereas in the EMEC, EM Barrel and HEC the pulse is injected at the calorimeter electrodes[3].

Between LHC fills, electronic calibration studies of the LAr calorimeters may be performed. There are three types of calibration runs that may be undertaken during these studies: delay runs, ramp runs, and pedestal runs. Pedestal runs are used to record samples in the absence of any signal, and thus can be used to obtain the RMS of the electronics noise in the channel and the autocorrelation function of the noise. The noise autocorrelation function is used in the derivation of the OFCs, while the noise RMS is taken as the pedestal value, which is subtracted from pulse samples during reconstruction

of the pulse peak.

The calibration pulse is controlled by a 16-bit Digital-to-Analog Converter (DAC)[25]. In ramp runs, the amplitude of the injected calibration pulse is varied (“ramped”), and OFCs are then applied in order to reconstruct the pulse peak. This allows the relationship between the input current signal (in DAC) and the reconstructed pulse peak (in ADC) to be measured. A linear fit is performed to the (ADC,DAC) data, and the slope, R (in units of DAC/ADC), is extracted. Thus, the factor of R in equation 1.15 functions as an ADC→DAC conversion factor. The amplitude of the DAC signal and the peak value of the injected current pulse are related by the factor $F_{\text{DAC} \rightarrow \mu\text{A}}$, which depends on the specifics of the calibration board. The product $F_{\text{DAC} \rightarrow \mu\text{A}} R$ thus acts as an ADC→ μA conversion factor for calibration pulses.

However, signal pulses arising from ionisation have different shapes to the injected calibration pulses. Ionisation pulses are triangular, having a peak proportional to the number of ionisation electrons produced in the active region of the calorimeter cell and dropping to zero after the drift time has elapsed, whereas the injected calibration pulses are shaped like decaying exponentials. This has an effect during the shaping. For example, in the case where an injected calibration pulse and an ionisation pulse both have the same initial peak current, the amplitude of the calibration pulse after shaping will be slightly lower than that of the ionisation pulse (as illustrated in figure 1.18).

Delay runs allow the pulse shapes to be measured. In delay runs, the calibration pulse is delayed (with respect to the TTC clock) by multiples of 1 ns. This effectively allows the shaped calibration pulse to be sampled at 1 ns intervals, which gives an accurate measurement of the shape of the calibration pulse. This information may then be used to infer the final shape of pulses originating from ionisation[4], which may then be used (together with the noise autocorrelation information obtained from pedestal runs) to derive the OFCs used for data taking at ATLAS. The factor $M_{\text{phys}}/M_{\text{calib}}$ describes the ratio of the shaped ionisation pulse amplitude to that of the shaped calibration pulse

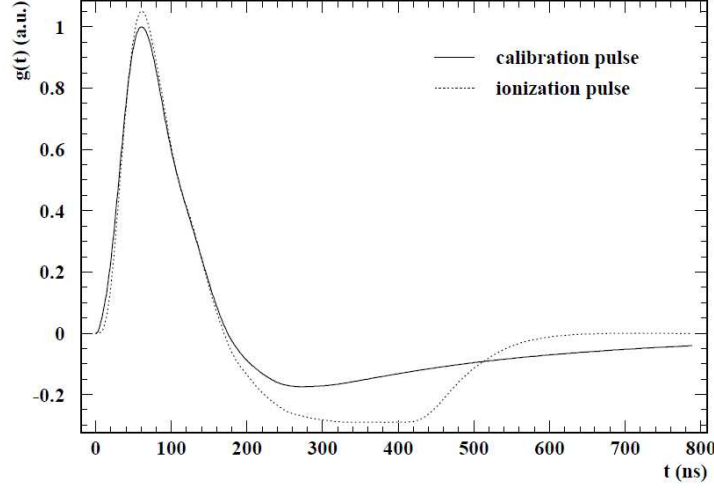


Figure 1.18: Calibration and ionisation pulse shapes for an EMB channel, after shaping. Prior to shaping, the peak current of the two pulses were equal [4].

amplitude, for cases in which both pulses have the same peak current prior to shaping. This factor corrects for the effect of pulse shaping, and thus allows the calibration factors (which are derived from calibration pulses) to be used for the calibration of ionisation pulses.

For the FCal, the calibration is based off testbeam studies rather than derived using calibration pulses. The ADC2MeV value obtained from testbeam is used to derive values of $F_{\mu A \rightarrow \text{MeV}}$ and $F_{\text{DAC} \rightarrow \mu A}$ that are appropriate for the electronics used in ATLAS. As the calibration is not derived from calibration pulses, the factor $\frac{1}{M_{\text{phys}}/M_{\text{calib}}}$ is not needed. Pedestal runs are used to measure noise in the electronics, but pulse shapes from testbeam data are used in the calculation of the OFCs (delay runs are not taken for the FCal). Ramp runs are still used to obtain R .

1.2.7 Trigger and Data Acquisition

Collisions between proton bunches occur at ATLAS at a design rate of 40MHz, however the maximum rate at which events can be recorded is limited by computing resources and is presently ~ 400 Hz. The trigger system is designed to ensure that as many interesting

events are recorded as possible, while rejecting less interesting events that occur at high rates, as shown in figure ?? . The **ATLAS** trigger system consists of three consecutive levels: level one (L1), level 2 (L2), and the Event Filter (EF). The L1 trigger selects candidate events at a maximum rate of 75 kHz. Most of these events are subsequently rejected at L2, reducing the acceptance rate to 3.5 kHz. The final level of event rejection is done by the EF, which accepts events at the desired rate of ~ 400 Hz.

The L1 trigger utilises custom-built hardware that is located off the detector, and needs to decide whether to accept or reject the event within $2.5 \mu\text{s}$ of the corresponding bunch crossing. The level 1 trigger consists of three of three parts, L1 Calo, L1 Muon, and the Central Trigger Processor (CTP). The L1 Calo trigger is used to select electrons, jets, taus, and other high p_T objects (excluding muons), while the L1 muon trigger processes signals from the RPCs and TGCs of the Muon Spectrometer.

The CTP decides whether an event is accepted or rejected at L1. Trigger conditions are specified in a “menu”, each item of which is some combination of trigger items from L1 Calo and/or L1 Muon. The CTP also handles the prescales on these menu items, which are used to control the bandwidth allowed for each item and keep the L1 acceptance rate at the desired level. For a menu item with a prescale of 50, one event will be accepted at L1 for every fifty events that satisfy the trigger conditions associated with that menu item. Menu items associated with a rare or particularly interesting event topology may be given a prescale of one, in which case the event is accepted every time the trigger conditions are met. Frequently occurring or less interesting topologies (such as those containing low- p_T jets) are given higher prescales.

The CTP also receives input from specialised detectors, such as ALFA (Absolute Luminosity For ATLAS), LUCID (Luminosity measurement using a Cherenkov Integrating Detector), and the Minimum Bias Trigger Scintillators (MBTS). LUCID [26] and ALFA [27] are luminosity detectors located 17m and 240m from the **ATLAS** interaction point, respectively, and are used to measure the luminosity delivered to **ATLAS**. The MBTS is

used to select “minimum bias” events: the thresholds required to accept these events are very low, and so collision events are selected with minimal bias. These events are typically soft inelastic scatterings. The MBTS consists of tiles of scintillating polystyrene that are 2cm thick. There are 16 of these tiles mounted on the outer wall of each end-cap cryostat (on the side closest to the interaction point), covering the pseudorapidity range $2.09 < |\eta| < 3.84$. Early studies of the MBTS showed it to be very efficient, with an efficiency of over 99% for selecting events in which there were at least 3 tracks with $p_T > 100\text{MeV}$ [28]. Because of its high efficiency and low bias, the MBTS trigger was used as a reference when determining the efficiency of the jet triggers used in the inclusive jet and dijet cross section measurements, as discussed in section ???. The distribution of charged particles obtained from minimum bias events recorded at ATLAS is plotted in figure 1.19. Note that the distribution is roughly uniform in η . Due to the nonlinear relationship between η and the polar angle, θ , a fixed interval $\Delta\eta$ corresponds to a smaller angular interval at high η than at low η . For example, one side of the EM Barrel has a length of 3.2 metres and covers the region $0 < \eta < 1.475$, while the FCal has an outer radius of $\sim 450\text{mm}$ and covers the region $3.2 < \eta < 4.9$: the FCal covers a larger pseudorapidity interval in a much smaller area. As the distribution of particles produced in minimum bias events varies slowly in η , detectors covering higher values of η will be subject to a higher flux of particles than detectors located at low η . The effects of pile up are thus more significant for the FCal and end-cap calorimeters than for the barrel calorimeters.

The time available for the L1 decision is too short for L1 Calo to consider the information from individual calorimeter cells. Cell information is stored in the detector electronics, and only read out when an L1 accept signal is received from the CTP. Of the $2.5\ \mu\text{s}$ available at L1, the decision is usually made within $2.1\ \mu\text{s}$. However, a large fraction of this time is taken up by the transit time for signals to propagate between the trigger hardware and the detector, while L1 Calo processes events in less than 1

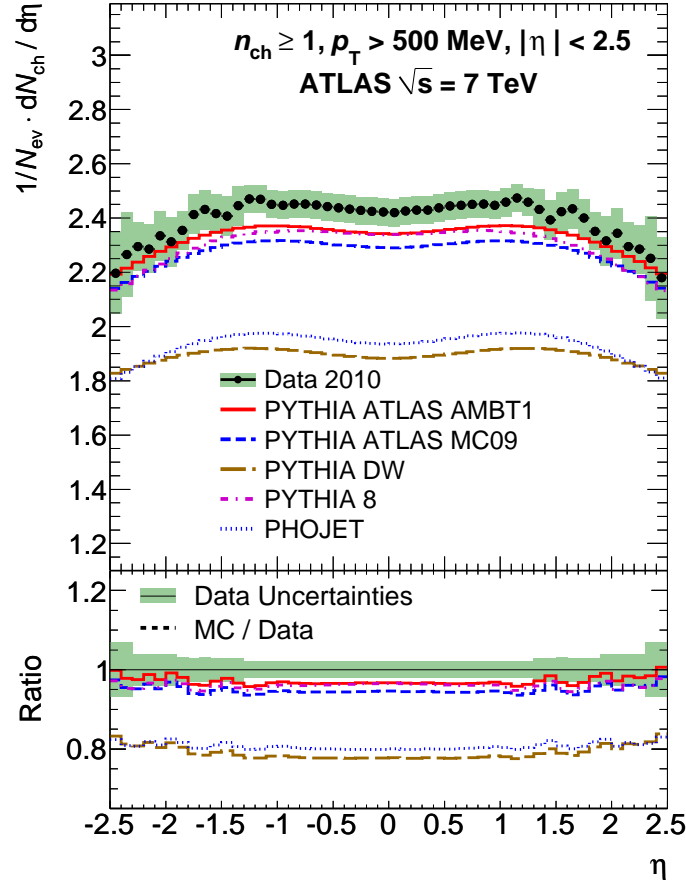


Figure 1.19: Distribution of charged particles produced in minimum bias events[5]. The plot shows data measured at ATLAS, as well as predictions obtained from Monte Carlo simulations using a variety of tunes. Note that the plot only covers the region $-2.5 < \eta < 2.5$, as Inner Detector coverage is limited to this interval.

μs . Instead of relying on cell information, calorimeter signals are instead processed into “trigger towers”, which are then sent as input to L1 Calo. Trigger towers are formed from analog sums of readout channel signals. In the Tile calorimeter, a trigger tower is formed by summing the signals from five channels. In the LAr calorimeters, the first two stages of summation are carried out on the FEBs, while the remaining addition is carried out on dedicated Tower Builder Boards (for the EMB and EMEC) or Tower Driver Boards (for the HEC and FCal)[29]. In the barrel and end-cap regions ($|\eta| < 3.2$), the trigger towers have a granularity 0.1×0.1 in η and ϕ , whereas in the FCal the trigger towers

have a granularity of approximately 0.4×0.4 .

The level 1 central jet trigger combines 2×2 blocks of trigger towers to form “jet elements”, which then have a granularity of 0.2×0.2 in $\eta - \phi$ space. A sliding window algorithm[30] is then used to identify jets. The window consists of a 4×4 grid of jet elements, and a jet is identified if the total transverse energy within the window exceeds a given threshold. For example, the “L1_J10” algorithm requires the transverse energy (at the EM scale) in the window to exceed 10 GeV. Additionally, the 2×2 cluster of jet elements in the centre of the window is required to be a local maximum; that is, the central cluster must have a transverse energy greater than that of any other 2×2 block of jet elements within the window.. If these criteria are met, then the event is accepted by the jet algorithm. The 0.4×0.4 area of $\eta - \phi$ at the centre of the window is then identified as a “Region of Interest” (ROI), and is passed on to any relevant L2 trigger algorithms.

The forward jet trigger is used to identify jets in the region $|\eta| > 3.2$, and operates independently of the central jet trigger. While the central jet trigger uses information from the EM Barrel, tile, EMEC and HEC calorimeters, only the forward jet trigger uses information from the FCal. Trigger towers in the FCal have a granularity of $\sim 0.4 \times 0.4$ in $\eta - \phi$, which is coarser than in other calorimeters. A jet element is then formed by summing all FCal trigger towers in η , such that the jet element has dimensions 1.6×0.4 in η and ϕ , respectively[30]. Jets are then identified using the same sliding window algorithm that is used by the central jet trigger[31].

At L2, the trigger decision needs to be made within 40ms. This interval is sufficient for cell-based methods to be used, although only cells within the region of interest (typically about 2% of the detector) are read out. A cone-based algorithm is used for jet identification: a cone of fixed radius $\Delta R = \sqrt{\Delta\eta^2 + \Delta\phi^2}$ is positioned at the centre of the RoI. Energy weighted values of η and ϕ are obtained by summing cells within the cone, and the centre of the cone is then moved to these coordinates. This process is

carried out a predetermined number of times.

At the EF level, 4.0s of processing time is available, and so algorithms similar to those used for offline reconstruction (described in section ??) may be used at the trigger level. Note that EF algorithms for jet triggers were not online while the data used in this thesis was being recorded, and so the trigger studies presented in section ?? focus on jet triggers at L1 and L2.

Bibliography

- [1] G. Aad et al. The ATLAS Experiment at the CERN Large Hadron Collider. *JINST*, 3:S08003, 2008.
- [2] Bernard Aubert et al. Development and construction of large size signal electrodes for the ATLAS electromagnetic calorimeter. *Nucl. Instrum. Meth.*, A539:558–594, 2005.
- [3] A Artamonov et al. The ATLAS Forward Calorimeter. *J. Instrum.*, 3:P02010, 2008.
- [4] D. Banfi, M. Delmastro, and M. Fanti. Cell response equalisation of the ATLAS electromagnetic calorimeter without the direct knowledge of the ionisation signals. *Journal of Instrumentation*, 1(08):P08001, 2006.
- [5] G. Aad et al. Charged-particle multiplicities in pp interactions measured with the ATLAS detector at the LHC. *New J.Phys.*, 13:053033, 2011.
- [6] (ed.) Evans, Lyndon and (ed.) Bryant, Philip. LHC Machine. *JINST*, 3:S08001, 2008.
- [7] Michael Benedikt et al. A walk through the LHC injector chain, 2005. <http://cdsweb.cern.ch/record/794393/pages>, CERN, Geneva, 21 - 23 Mar 2005.
- [8] S. Chatrchyan et al. The CMS experiment at the CERN LHC. *JINST*, 3:S08004, 2008.

- [9] G. Aad et al. Performance of primary vertex reconstruction in proton-proton collisions at $\sqrt{s}=7$ TeV in the ATLAS experiment. Technical Report ATLAS-CONF-2010-069, CERN, Geneva, Jul 2010.
- [10] G. Aad et al. Muon Momentum Resolution in First Pass Reconstruction of pp Collision Data Recorded by ATLAS in 2010. Technical Report ATLAS-CONF-2011-046, CERN, Geneva, Mar 2011.
- [11] R. Wigmans. *Calorimetry: Energy Measurement in Particle Physics*. International Series of Monographs on Physics. Clarendon Press, 2000.
- [12] C. Caso et al. Review of particle physics. Particle Data Group. *Eur.Phys.J.*, C3:1–794, 1998.
- [13] J. Beringer et al. Review of particle physics. Particle Data Group. *Phys. Rev.*, D86, 2012.
- [14] R. Wigmans. Calorimetry. *Scientifica Acta*, 2(1):18, 2008.
- [15] M. Derrick et al. Design and construction of the ZEUS barrel calorimeter. *Nuclear Instruments and Methods in Physics Research Section A: Accelerators, Spectrometers, Detectors and Associated Equipment*, 309(120132):77 – 100, 1991.
- [16] Christian W. Fabjan and Fabiola Gianotti. Calorimetry for particle physics. *Rev. Mod. Phys.*, 75:1243–1286, Oct 2003.
- [17] ATLAS liquid-argon calorimeter: Technical Design Report. Technical report, Geneva, 1996.
- [18] ATLAS tile calorimeter: Technical Design Report. Technical report, Geneva, 1996.
- [19] D. M. Gingrich et al. Construction, assembly and testing of the ATLAS hadronic end-cap calorimeter. *JINST*, 2:P05005, 2007.

- [20] J. Colas, M. Pripstein, and W. A. Wenzel. The electrostatic transformer. *Nuclear Instruments and Methods in Physics Research A*, 294:583–590, September 1990.
- [21] John Paul Archambault et al. The simulation of the ATLAS liquid argon calorimetry. 2009.
- [22] N J Buchanan et al. Design and implementation of the Front End Board for the readout of the ATLAS liquid argon calorimeters. *JINST*, 3(03):P03004, 2008.
- [23] W.E. Cleland and E.G. Stern. Signal processing considerations for liquid ionization calorimeters in a high rate environment. *Nuclear Instruments and Methods in Physics Research Section A: Accelerators, Spectrometers, Detectors and Associated Equipment*, 338(2-3):467 – 497, 1994.
- [24] Laurence W. Nagel and D.O. Pederson. SPICE (Simulation Program with Integrated Circuit Emphasis). Technical Report UCB/ERL M382, EECS Department, University of California, Berkeley, Apr 1973.
- [25] J Ye. Electronics of the Atlas Liquid Argon Calorimeter and its Precision Calibration. Technical Report ATL-LARG-PROC-2009-006. ATL-COM-LARG-2009-020, CERN, Geneva, Jun 2009. June 17, 2009.
- [26] M. Bruschi. The ATLAS luminosity monitor. *Nuclear Instruments and Methods in Physics Research Section A: Accelerators, Spectrometers, Detectors and Associated Equipment*, 623(1):371 – 373, 2010. [1st International Conference on Technology and Instrumentation in Particle Physics](#).
- [27] Peter Jenni et al. *ATLAS Forward Detectors for Measurement of Elastic Scattering and Luminosity*. Technical Design Report. CERN, Geneva, 2008.
- [28] Lauren Tompkins. Performance of the ATLAS Minimum Bias Trigger in p-p collisions at the LHC. 2010.

- [29] N. J. Buchanan et al. ATLAS liquid argon calorimeter front end electronics. *JINST*, 3(09):P09003, 2008.
- [30] R. Achenbach et al. The ATLAS level-1 calorimeter trigger. *JINST*, 3:P03001, 2008.
- [31] Uli Schäfer and Samuel Silverstein. ATLAS level-1 Calorimeter Trigger Jet/Energy Module Project Specification, October 2012. <https://edms.cern.ch/file/326674/1.2d/JEMspec12d.pdf>.